

Ordnance/Clutter Discrimination Based on Target Eigenvalue Analysis

Stephen J. Norton and I. J. Won

Geophex, Ltd., 605 Mercury Street, Raleigh, NC 27603

Ernesto R. Cespedes

US Army Engineer Research and Development Center,
3909 Halls Ferry Road, Vicksburg, MS 39180

Received January 30, 2001; revised April 17, 2001

A procedure is described for deriving a quantitative measure of the "ordnance-likeness" of an unknown target from electromagnetic induction data, which thus can be used as a clutter discriminant. This parameter provides a measure of the axial symmetry and aspect ratio of the target and is formed by taking the ratio of the eigenvalues of the target's magnetic polarizability tensor. The eigenvalues are derived by measuring the matrix elements of the polarizability tensor from above-ground spatial data and then performing an eigenvalue decomposition of this tensor. The method is linear, and does not require a nonlinear parameter search. The eigenvalue ratio is smaller than one for objects that are symmetric and long (ordnance-like) and greater than one for objects that are flat and/or irregular in shape (clutter-like). This ratio is independent of the orientation of the target. The procedure is demonstrated using data derived from samples of metallic clutter and ordnance-like objects (i.e., cylinders, sections of pipe and actual ordnance) at different orientations.

Key Words. Unexploded ordnance, electromagnetic induction, subsurface detection, target discrimination, target recognition.

1. Introduction

A critical problem identified by the Department of Defense is the remediation of military ranges contaminated with a mixture of buried unexploded ordnance (UXO) and ordnance fragments (clutter). As a general rule, a large majority of the objects detected are not UXO, so that an effective means of discriminating between true UXO and clutter would result in

a significant savings in remediation costs. Geophex, Ltd., has in recent years developed a series of broadband electromagnetic induction (EMI) sensors for detecting and characterizing buried conducting anomalies [1-3]. In particular, the GEM-3 sensor [2], employing co-axial coils, has been shown to be effective in detecting and identifying buried UXO. This sensor is well suited for this purpose because of its multi-frequency capability and its compact spatial footprint.

Several previous approaches to the UXO-characterization problem have been based on an attempt to fit a dipole model to EMI data recorded at multiple points on the surface [4,5]. Typically, the target is assumed to have axial symmetry. In one version, the dipole-fitting algorithm performs a nonlinear search for seven parameters that characterize the target: the x , y and z coordinates of its centroid, two angles defining its orientation, and two eigenvalues characterizing its longitudinal and transverse responses. A related technique has been independently proposed for the purpose of landmine identification [6].

Here we describe an approach that has the same objective of characterizing the target, but is linear and non-iterative. This has several advantages over nonlinear search schemes: (1) the method is computationally fast, requiring a single linear least-squares inversion followed by an eigen-decomposition of a 3 by 3 matrix; (2) the method avoids pitfalls associated with iterative, nonlinear algorithms, such as sensitivity to starting values and the possibility of getting trapped in local minima; and (3) a sensitivity analysis can be conveniently performed using the singular-value decomposition to assess the "observability" of the matrix elements of the polarizability tensor for a given set of spatial samples.

When the sensor/target separation is greater than a few target lengths, a quite accurate model of the interaction of the fields with the target is given by the lowest order term in a multipole expansion of the target response (the dipole term). Using reciprocity principles, this term can be expressed in the following form [7-9]:

$$emf_R = \mathbf{H}_T \cdot \mathbf{P} \cdot \mathbf{H}_R \quad (1)$$

where emf_R is the emf induced in the receiving coil, \mathbf{H}_T is the incident magnetic field at the location of the target (i.e., the field in the absence of the target) generated by the transmitting coil, and \mathbf{H}_R is the incident field generated by the receiving coil if it were used as a transmitter. In Eq. (1), the target is characterized by \mathbf{P} , which is a 3 by 3 complex, symmetric matrix known as the magnetic polarizability tensor. As noted, Eq. (1) is the lowest-order term in a multipole expansion of the target response; the second term is smaller than this term by a factor on the order of $(r/d)^2$, where d is the characteristic dimension of the target and r is the distance between the target

and sensor. As a consequence, the approximation expressed by Eq. (1) is expected to be reasonable at target ranges three or four times the target size, or greater.

For a monostatic system (such as the GEM-3), the transmitting and receiving fields, \mathbf{H}_T and \mathbf{H}_R , are incident from the same direction; defining this direction by the unit vector \mathbf{n} , Eq. (1) may be written

$$emf_R = f(r)\mathbf{n} \cdot \mathbf{P} \cdot \mathbf{n} \quad (2)$$

where $f(r)$ is a range-dependent factor, which can be regarded as unknown. Our only assumption is that $f(r)$ depend on r and not on frequency.

For convenience, Eq. (2) can be written in the form

$$emf_R = \mathbf{n} \cdot \mathbf{S} \cdot \mathbf{n} \quad (3)$$

where we define the modified polarizability tensor

$$\mathbf{S} = f(r)\mathbf{P} \quad (4)$$

2. Eigenvalue Analysis

Our procedure is to measure the matrix elements of \mathbf{S} from data recorded at multiple positions on the surface. Diagonalizing \mathbf{S} then gives its eigenvalues; the latter contain intrinsic geometric information about the target, which is independent of the target orientation.

In measuring the matrix elements of \mathbf{S} , the first step is to compute the incident unit vector \mathbf{n} at the target location. In principle, this requires knowledge of the target position relative to the sensor head; one can then compute the incident field \mathbf{H} at the target, from which its direction $\mathbf{n} = \mathbf{H}/|\mathbf{H}|$ can be derived. The target position (its depth and transverse coordinates) can be estimated, for example, by fitting the target response to a dipole model using either EMI or magnetometry data. Alternatively, an approximate estimate of the target's transverse coordinates can be obtained from the peak of the surface field anomaly, and an estimate of its depth can be derived from the half-width of the surface anomaly. The latter method was used in the current work. Note that, although the calculated amplitude of the field at the target position is quite sensitive to the target's estimated depth, the field direction, denoted by \mathbf{n} , is less so. Thus, some uncertainty in the target location for the purpose of computing \mathbf{n} is probably tolerable. This appears to have been borne out by the experimental work reported here.

Once the unit vector \mathbf{n} has been computed for each sensor position, we obtain the matrix elements of \mathbf{S} from the spatially sampled data using a

method described in the Appendix. The matrix \mathbf{S} may be written

$$\mathbf{S} = \begin{pmatrix} s_{11} & s_{12} & s_{13} \\ s_{21} & s_{22} & s_{23} \\ s_{31} & s_{32} & s_{33} \end{pmatrix} \quad (5)$$

This matrix is symmetric, as reciprocity arguments dictate, so that only six independent (complex) matrix elements define it. As a result, six inphase and quadrature observations performed at six different angles of incidence (i.e., corresponding to six different unit vectors \mathbf{n}) are sufficient to recover these elements and hence \mathbf{S} . In general, more than six spatial measurements are desirable and the elements of \mathbf{S} may be estimated by least squares. The next step is to compute the eigenvalues of \mathbf{S} , denoted by $\lambda_1(\omega)$, $\lambda_2(\omega)$ and $\lambda_3(\omega)$, for all measured frequencies ω . Thus, diagonalizing \mathbf{S} gives

$$\mathbf{S}(\omega) = \mathbf{O}\Lambda(\omega)\mathbf{O}^T \quad (6)$$

where \mathbf{O} is a rotation matrix, and

$$\Lambda(\omega) = \begin{pmatrix} \lambda_1(\omega) & 0 & 0 \\ 0 & \lambda_2(\omega) & 0 \\ 0 & 0 & \lambda_3(\omega) \end{pmatrix} \quad (7)$$

As noted, the (complex) eigenvalues $\lambda_i(\omega)$ characterize the target shape and are independent of orientation. The Appendix contains a description of the procedure for computing the matrix elements \mathbf{S} from EMI measurements recorded above ground. Suppose, in the following, that the eigenvalues $\lambda_i(\omega)$ have been derived in this manner for some unknown object.

Our approach is based on the observation that nearly all ordnance have an axis of symmetry, implying that $\lambda_1(\omega) \approx \lambda_2(\omega)$ if we choose the third axis as the symmetry axis. Thus, a general test for an object to be "ordnance-like" will be equality (or near equality) of two of its eigenvalues, which should differ significantly from the third eigenvalue. In practice, perfect equality of two of the eigenvalues will never occur due to departures from the dipole model defined by Eq. (1) and imperfections in the data (e.g., imperfect compensation for the influence of the soil).

Figure 1 shows the three eigenvalues, $\lambda_1(\omega)$, $\lambda_2(\omega)$ and $\lambda_3(\omega)$, measured from a 37 mm projectile plotted against frequency. Note that the two upper eigenvalue spectra are close together. These correspond to the two degenerate transverse responses of the target, whereas the lower most eigenvalue spectrum corresponds to the longitudinal target response. This figure is characteristic of axial symmetric objects with an aspect ratio greater than one, such as UXO-like objects. In contrast, Figure 2 shows the eigenvalue spectra measured from a bent ferrous fragment (clutter). In this case, the

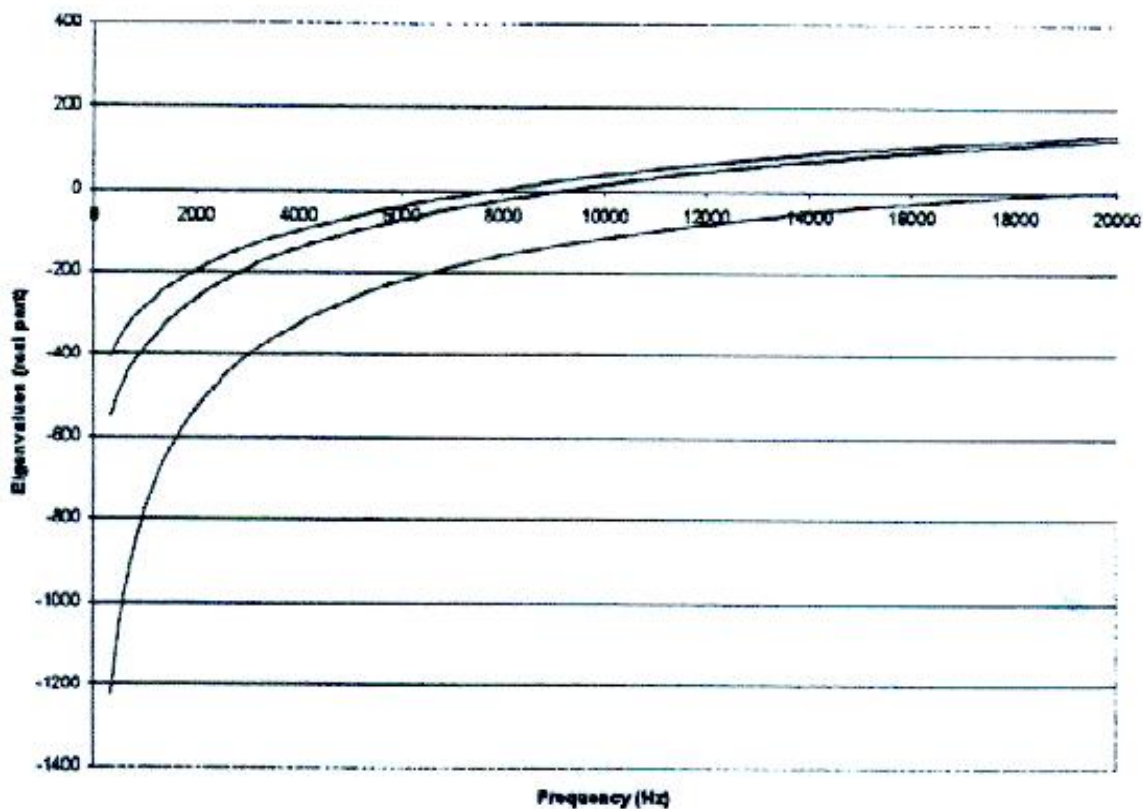


Figure 1. Measured inphase eigenvalue spectra of 37 mm projectile.

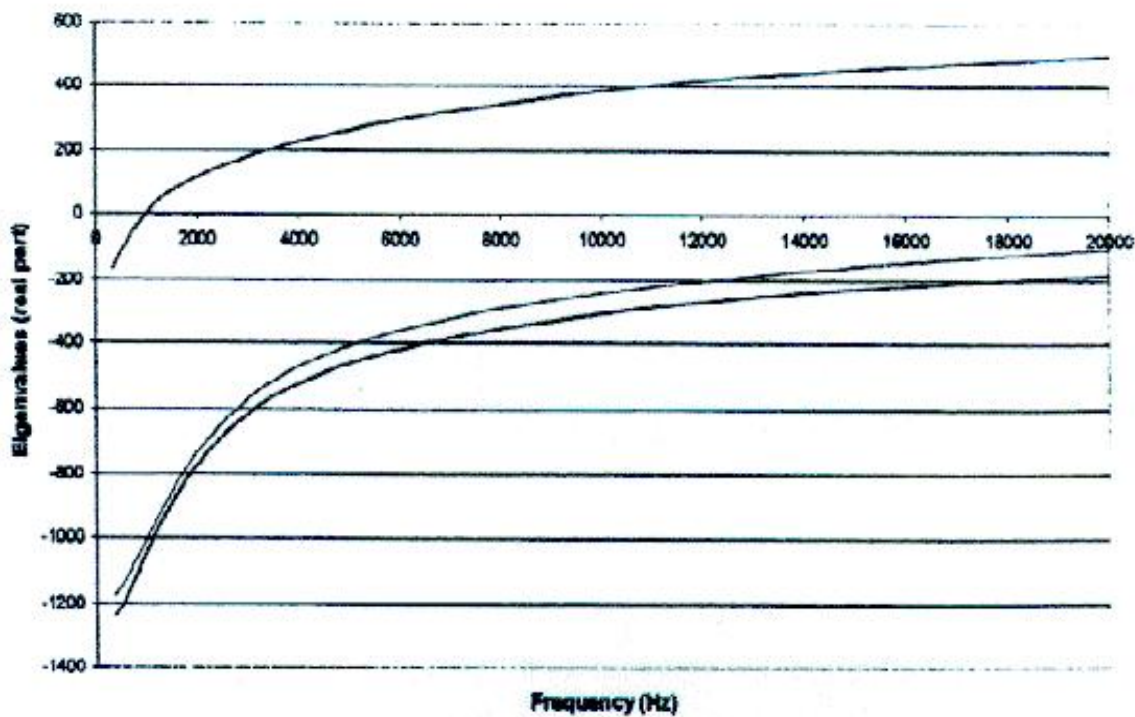


Figure 2. Measured inphase eigenvalue spectra of piece of ferrous clutter.

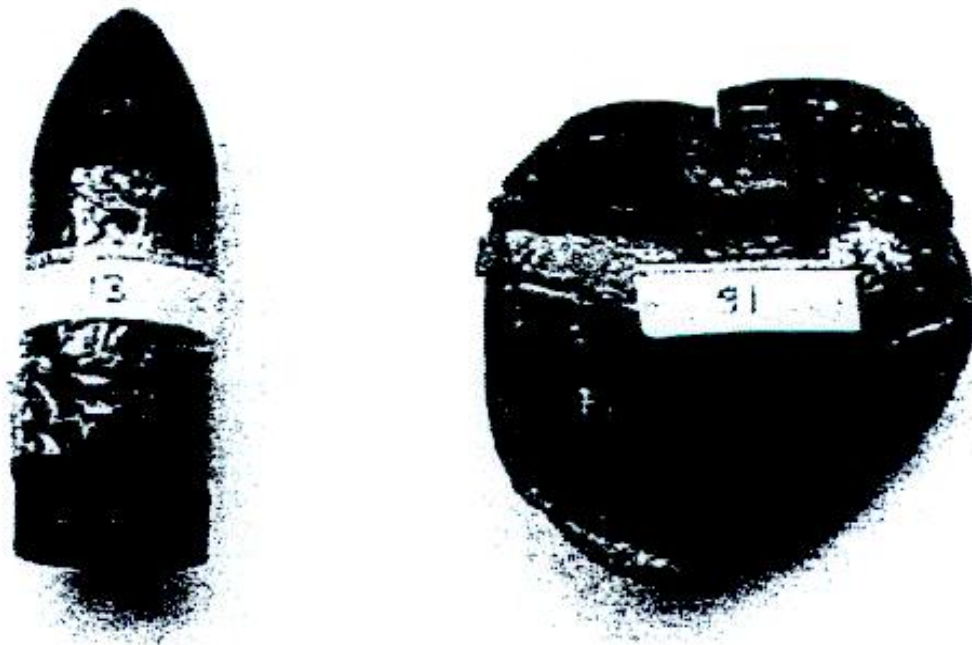


Figure 3. On the left is a 37 mm projectile and on the right is a piece of ferrous clutter.

two lower eigenvalue spectra are close together, which is characteristic of objects with an aspect ratio smaller than one. Figure 3 shows a photograph of these two objects.

A convenient measure of this difference in aspect ratio can be obtained by taking the real part of each eigenvalue, denoted by $\lambda_1^R(\omega)$, $\lambda_2^R(\omega)$, $\lambda_3^R(\omega)$, sorting the eigenvalues at each frequency, such that $\lambda_1^R(\omega) < \lambda_2^R(\omega) < \lambda_3^R(\omega)$, and then forming the ratio

$$\rho_R(\omega) = \frac{\lambda_3^R(\omega) - \lambda_2^R(\omega)}{\lambda_2^R(\omega) - \lambda_1^R(\omega)} \quad (8)$$

For objects with an aspect ratio much greater than one, $\lambda_1^R(\omega) \ll \lambda_2^R(\omega) \approx \lambda_3^R(\omega)$, which implies $\rho_R(\omega) \ll 1$, and for objects with an aspect ratio much less than one, $\lambda_1^R(\omega) \approx \lambda_2^R(\omega) \ll \lambda_3^R(\omega)$, which implies $\rho_R(\omega) \gg 1$. For objects with an aspect ratio near one, $\rho_R(\omega) \approx 1$. For convenience, we compute the log of $\rho_R(\omega)$, so that $\log[\rho_R(\omega)] < 0$ for UXO-like objects and $\log[\rho_R(\omega)] \geq 0$ for objects that resemble clutter. A similar ratio can be

Table 1. The Label under "Orientation" Indicates the Direction along the Longer Dimension of the Object. The 37mm Projectile and Clutter #91 are Shown in Figure 3

Object	Type	Orientation	Dimensions
37 mm projectile	UXO	Vertical	3.5 cm diameter, 11 cm long
Steel cylinder	UXO-like	Vertical	2.5 cm diameter, 10 cm long
Aluminum cylinder	UXO-like	Vertical	2.5 cm diameter, 10 cm long
Aluminum cylinder	UXO-like	45 degrees	2.5 cm diameter, 10 cm long
Aluminum cylinder	UXO-like	Horizontal	2.5 cm diameter, 10 cm long
Aluminum disk	Clutter	Horizontal	12 cm diameter, thin
Aluminum disk	Clutter	Vertical	12 cm diameter, thin
Paint can lid	Clutter	Horizontal	15 cm diameter, thin
Crushed soda can	Clutter	Horizontal	6 cm diameter, 2.5 cm long
Coil of wire	Clutter	Horizontal	16 cm diameter, thin
Brass disk	Clutter	Horizontal	7.5 cm diameter, 2.5 cm long
Clutter #91	Clutter	Horizontal	irregular shaped ferrous steel, 10 cm × 11 cm
Aluminum box	Clutter	Horizontal	7.5 cm × 6 cm × 5 cm

formed using the imaginary parts of the eigenvalues, but this was found to be a less effective measure of symmetry and aspect ratio.

3. Experiments with UXO-Like Objects and Clutter

To demonstrate the above theory, the GEM-3 sensor was used to record multi-frequency data over a variety of targets, both clutter-like and UXO-like. In the latter category, we include cylinders, sections of pipe, and real UXO. In the first set of measurements, data were recorded on a test stand above the ground. The items examined are listed in Table 1. The center of the sensor head was moved relative to the center of the target on a 5 by 5 square grid of points, with a grid point spacing of 10 cm. The distance between the plane of the grid and the center of the target was 35 cm (the "depth"). The instrument was set to record eight frequencies simultaneously: 330, 570, 1100, 2070, 3810, 7050, 12,990, 20,010 Hz.

From the spatial data, the eigenvalues and the quantity $\log[\rho_R(\omega)]$ were computed for each object at all eight frequencies. Figure 4 shows $\log[\rho_R(\omega)]$ plotted as a function of frequency for the items listed in Table 1. We see that the spectra for the objects that are clutter-like have positive values, whereas the objects that are UXO-like have negative values, as predicted.

We also computed the ratio of the imaginary parts of the eigenvalues (obtained from the quadrature component of the data), as follows

$$\rho_I(\omega) = \frac{\lambda_3^I(\omega) - \lambda_2^I(\omega)}{\lambda_2^I(\omega) - \lambda_1^I(\omega)} \quad (9)$$

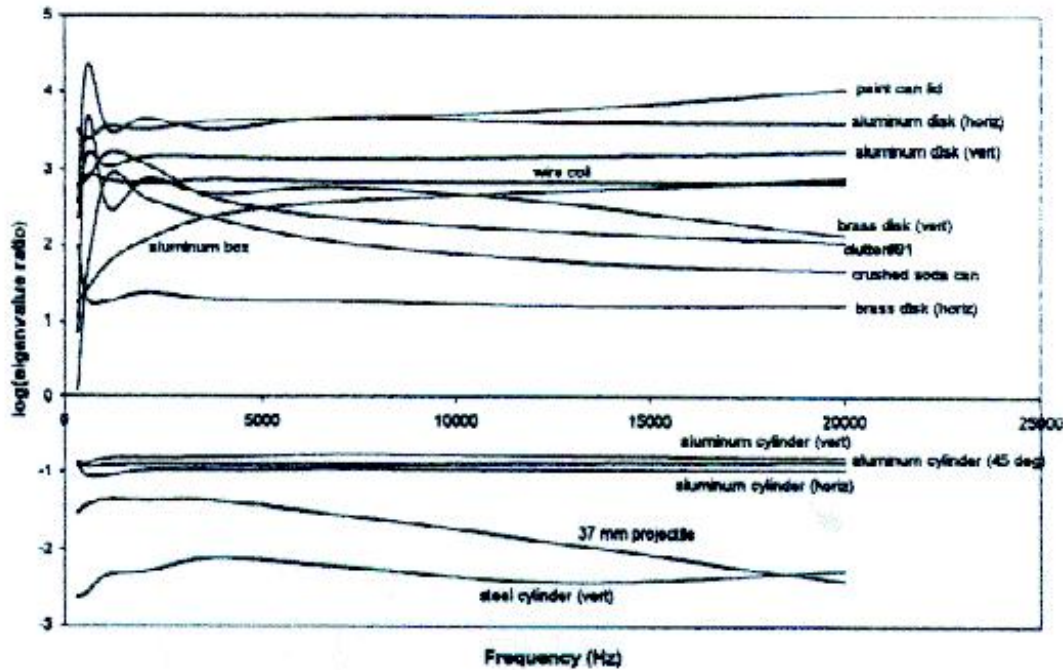


Figure 4. \log (ratio of eigenvalues).

where the “ I ” stands for imaginary part. This quantity was not found to be as effective in separating the UXO-like objects from clutter. This may be due in part to the fact that the quadrature component is a somewhat more complex function of frequency than the inphase component. In fact the imaginary parts of the three eigenvalues generally peak at three different frequencies, making interpretation of $\rho_I(\omega)$ more difficult than $\rho_R(\omega)$.

To obtain a single “UXO-likelihood” index, we computed the mean of the log ratios $\log[\rho_R(\omega)]$ over all frequencies, denoted by $\log[\bar{\rho}_R]$. Similarly, we let $\log[\bar{\rho}_I]$ signify the mean of $\log[\rho_I(\omega)]$. Figure 5 shows a 2-D plot of the points $(\log[\bar{\rho}_I], \log[\bar{\rho}_R])$, one point per target, where the horizontal axis is the $\log[\bar{\rho}_I]$ value and the vertical axis is the $\log[\bar{\rho}_R]$ value. In this figure, the letters C and U identify, respectively, a clutter-like item and a UXO-like item. Figure 6 is the same plot with more detailed labels. Note again that the clutter-like items all lie above the horizontal axis (positive $\log[\bar{\rho}_R]$), whereas the UXO-like items fall below this axis (negative $\log[\bar{\rho}_R]$). From these figures it is clear that the discriminatory power of the parameter $\rho_R(\omega_m)$ is much greater than that of $\rho_I(\omega_k)$.

As a more realistic test, measurements were performed over a second set of targets below ground, either buried or placed in a hole. These items are listed in Table 2. In this case, the sensor was moved to different points on a 5 by 5 grid on the surface with a grid point spacing of 12.5 cm. The frequencies were 150, 270, 510, 990, 1950, 3870, 7710, 11,430 Hz. The purpose of the in-ground test was to determine the sensitivity of the procedure

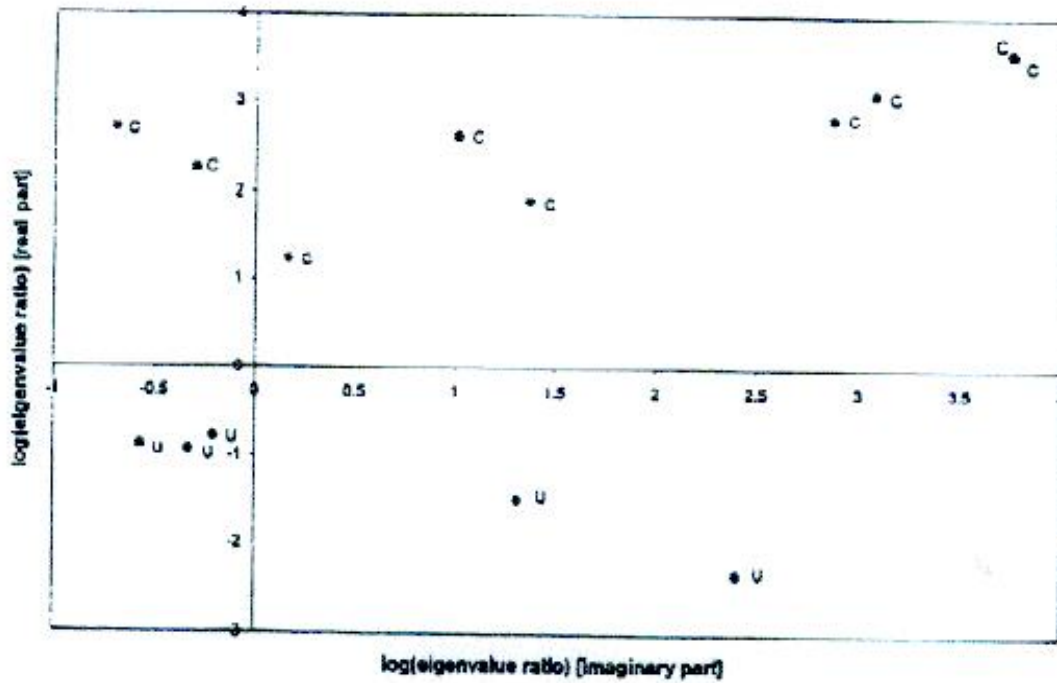


Figure 5. Quadrature vs. inphase log ratios.

to the influence of the ground. Previous measurements have shown that the ground contributes a significant offset in the inphase component of the measurement, which is a function of sensor height. The soil at the site was found to have a mean apparent conductivity of approximately 0.05 S/m and a mean apparent relative magnetic susceptibility of approximately 2×10^{-4} .

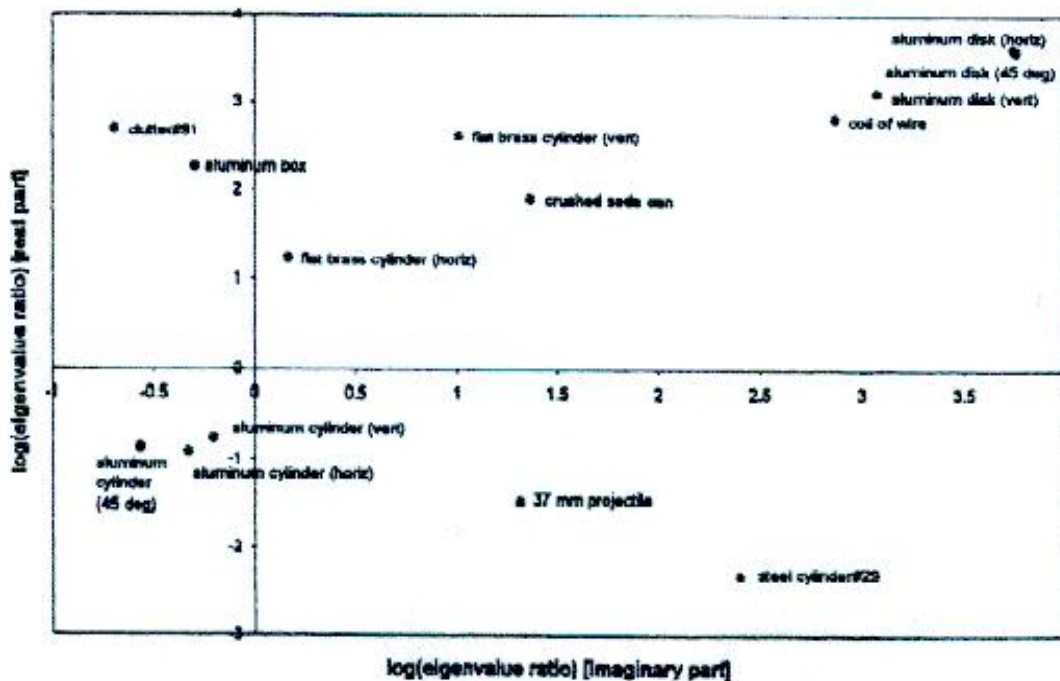


Figure 6. Quadrature vs. inphase log ratios.

Table 2. The (B) or (H) in the Column under "Type" Indicates Whether the Object Was Buried or Placed in a Hole. The Label under "Orientation" Indicates the Direction along the Longer Dimension of the Object

Object	Type	Orientation	Depth	Dimensions
30 mm projectile	UXO (H)	Vertical	20 cm	3 cm diam., 10 cm long
37 mm projectile	UXO (H)	Vertical	20 cm	3.7 cm diam., 11 cm long
57 mm projectile	UXO (H)	Vertical	20 cm	5.7 cm diam., 12 cm long
Steel cylinder #29	UXO-like (H)	Vertical	20 cm	2.5 cm diam., 10 cm long
Steel pipe #1	UXO-like (H)	Vertical	25 cm	2.5 cm diam., 10 cm long
Steel pipe #1	UXO-like (B)	Horizontal	15 cm	2.5 cm diam., 10 cm long
Steel pipe #3	UXO-like (B)	Vertical	35 cm	4 cm diam., 15 cm long
Steel pipe #4	UXO-like (B)	Horizontal	35 cm	5 cm diam., 10.5 cm long
Steel pipe #5	UXO-like (B)	Horizontal	35 cm	4 cm diam., 15 cm long
Steel pipe #6	UXO-like (B)	Horizontal	35 cm	4 cm diam., 15 cm long
Steel pipe #7	UXO-like (B)	Horizontal	35 cm	5 cm diam., 10.5 cm long
Steel pipe #8	UXO-like (B)	45 degrees	25 cm	4 cm diam., 15 cm long
Steel pipe #10	UXO-like (B)	Horizontal	15 cm	2.5 cm diam., 10 cm long
Steel pipe #M1	UXO-like (B)	Vertical	85 cm	7.5 cm diam., 45 cm long
Steel pipe #M3	UXO-like (B)	Horizontal	55 cm	6 cm diam., 30 cm long
Steel pipe #M4	UXO-like (B)	45 degrees	65 cm	6 cm diam., 30 cm long
Clutter #91	Clutter (H)	Vertical	25 cm	10 cm × 11 cm (steel)
Clutter #125	Clutter (H)	Vertical	25 cm	9 cm diam., 6 cm long (alum.)
Clutter #134	Clutter (H)	Vertical	25 cm	5 cm diam., 14 cm long (alum.)
Aluminum plate	Clutter (H)	45 degrees	30 cm	9 cm × 9 cm
Aluminum box	Clutter (H)	Horizontal	30 cm	7.5 cm × 6 cm × 5 cm
Crushed soda can	Clutter (H)	Horizontal	30 cm	7 cm diam., 2 cm long
Paint can lid (bent)	Clutter (H)	45 degrees	25 cm	15 cm diam.
Putty knife	Clutter (H)	Vertical	25 cm	18 cm × 8 cm
Short steel cylinder	Clutter (H)	Horizontal	30 cm	5 cm diam., 4 cm long
C-clamp (closed)	Clutter (H)	Vertical	30 cm	13 cm × 8 cm
C-clamp (open)	Clutter (H)	Vertical	30 cm	13 cm × 8 cm

In the in-ground test, the depth of the target was not assumed known a priori, but computed from the width of the surface field anomaly. This width was found by fitting a two-dimensional Gaussian surface to the field pattern sampled by the 2-D grid. The Gaussian surface was assumed to have two principal axes, each with a different standard deviation, and an arbitrary orientation. The algorithm performs a five parameter fit to the surface field pattern: the x and y coordinates of the center of the anomaly, the two Gaussian standard deviations, and the orientation angle of the Gaussian surface. The fitting procedure employed a Levenberg–Marquardt iterative least squares algorithm. The actual depth was found to be approximately 1.5 times the average of the two Gaussian standard deviations. This value was used as our depth estimate and was within about plus or minus 25% of the true target depth.

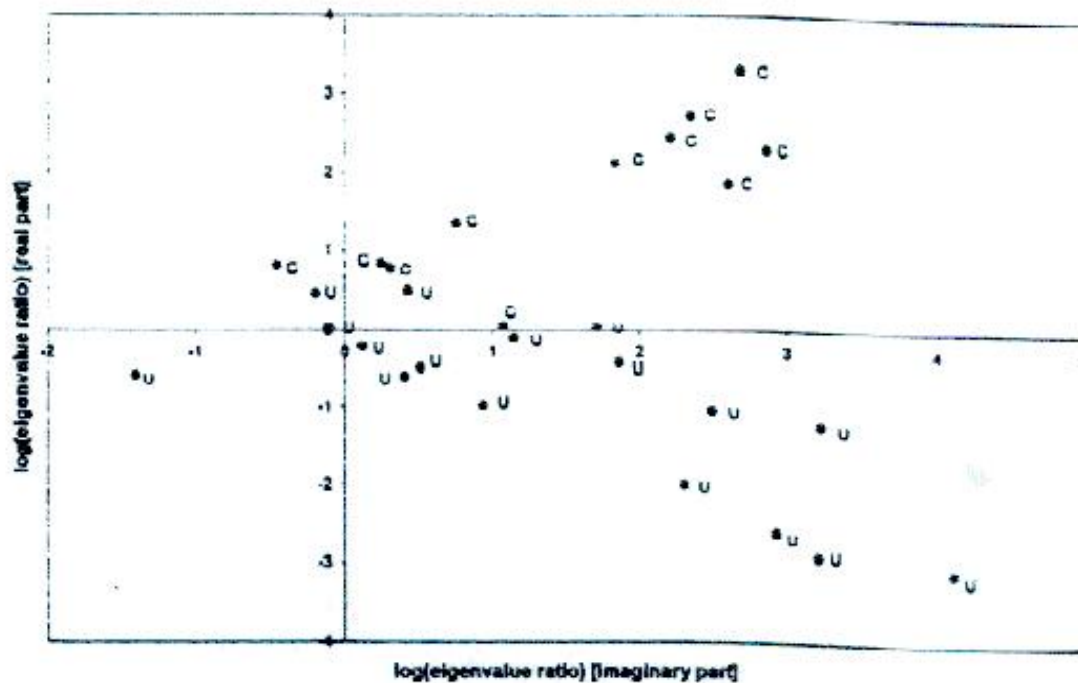


Figure 7. Quadrature vs. inphase log ratios.

Figure 7 shows the targets listed in Table 2 plotted in the $(\log[\tilde{\rho}_I], \log[\tilde{\rho}_R])$ plane, where again C and U identify clutter and UXO-like items. Figure 8 is the same plot with more detailed labels. Note that most of the UXO-like items are separated from the clutter by the horizontal axis,

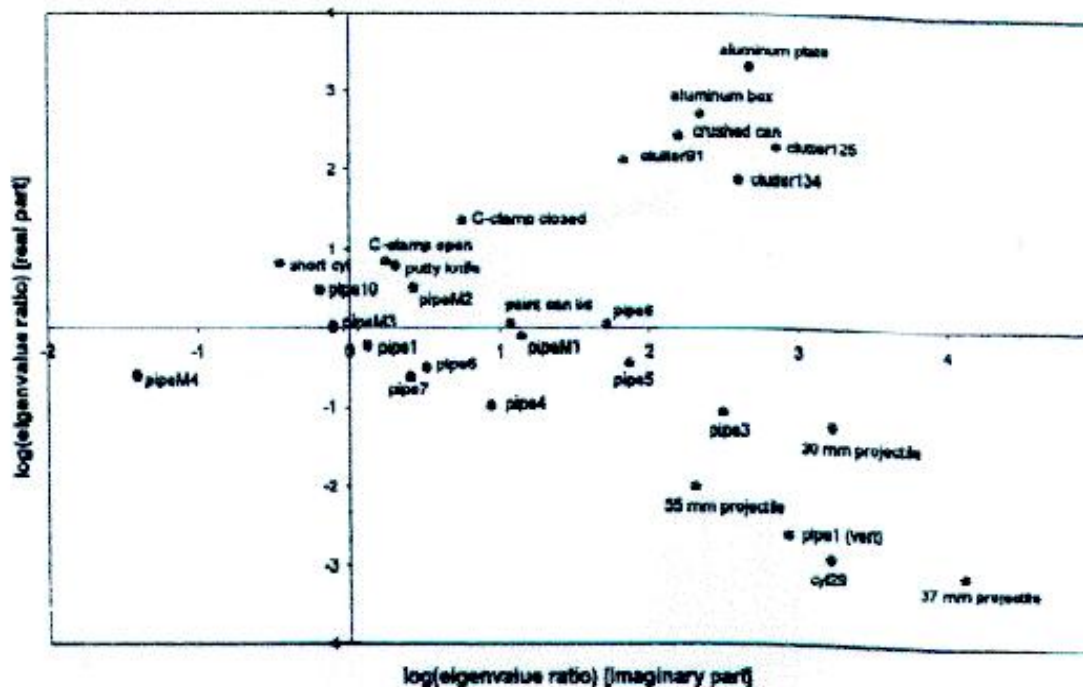


Figure 8. Quadrature vs. inphase log ratios.

but there are a few errors. If the UXO/clutter separation threshold is set at $\log[\rho_R] = 0$, all 10 of the clutter items are correctly classified, but of the 17 UXO-like items, 4 are misclassified as clutter. One of these misclassifications (pipe #10) was due to a particularly poor depth estimate due to the fact that this target was very shallow. All of the misclassified objects are fairly close to the threshold $\log[\rho_R] = 0$, and if this threshold were increased to $\log[\rho_R] = 1$, then all the UXO-like targets would have been correctly classified with 4 false alarms (i.e., 4 clutter items declared UXO-like). From another point of view, the projection of the points onto the vertical axis gives rise to two well-separated distributions, although the two distributions have some overlap. This means that most, but not all, items will be correctly classified. Projection onto the horizontal axis does not appear to produce a meaningful separation of the UXO and clutter, but more data are needed to establish this.

Several reasons for the imperfect classification are possible:

- (1) For targets buried in the ground, exact correction for the influence of the soil on the inphase component of the measured field is not possible. We attempted to subtract the background due to the ground using the average of the values recorded at the four corners of the grid. This worked reasonably well, but an investigation of more effective background removal strategies would be worthwhile and is under study.
- (2) The estimated target depth based on the surface anomaly width is fairly inaccurate. A more accurate depth estimation procedure based on fitting to a dipole model using either the EMI data or magnetometry data should improve performance.
- (3) The spacing of the grid points was probably not optimal for all targets. For larger, deeper targets, the grid point spacing should be increased to cover the most significant part of the surface anomaly. Smaller, shallower targets require a smaller grid spacing.

4. Conclusion

We have begun a preliminary investigation of a technique for separating UXO-like objects from clutter using spatially-sampled EMI data. Thus far, the results are encouraging, but more testing on a wider variety of UXO and clutter items is needed. It is expected that classification errors can be reduced with a more effective background-removal strategy and a more accurate method of estimating target depth.

Acknowledgments

This work was funded in part by the US Army Corps of Engineers' Installation Restoration Research Program.

Appendix

To describe the procedure for computing the elements of the matrix \mathbf{S} from data, we employ the following dyadic expansion of \mathbf{S}

$$\mathbf{S} = \sum_{i=1}^3 \sum_{j=1}^3 s_{ij} \mathbf{x}_i \mathbf{x}_j \quad (\text{A1})$$

where \mathbf{x}_1 , \mathbf{x}_2 and \mathbf{x}_3 are any set of convenient orthogonal unit vectors. As noted, because $s_{ij} = s_{ji}$, \mathbf{S} is defined by the six independent elements $\{s_{11}, s_{22}, s_{33}, s_{12}, s_{13}, s_{23}\}$.

Suppose N measurements are made above ground, denoted by $emf_R^{(k)}$, with corresponding unit vectors \mathbf{n}_k , $k = 1, \dots, N$. We then obtain by substituting Eq. (A1) into (3), the following N equations in the six unknowns $\{s_{11}, s_{22}, s_{33}, s_{12}, s_{13}, s_{23}\}$

$$emf_R^{(k)} = \sum_{i=1}^3 \sum_{j=1}^3 s_{ij} K_{ij}^{(k)}, \quad k = 1, \dots, N \quad (\text{A2})$$

where

$$K_{ij}^{(k)} \equiv (\mathbf{n}_k \cdot \mathbf{x}_i)(\mathbf{n}_k \cdot \mathbf{x}_j) \quad (\text{A3})$$

The N linear equations given by Eq. (A2) can then be solved to recover the six elements $\{s_{11}, s_{22}, s_{33}, s_{13}, s_{23}\}$. If N is greater than six, the resultant over-determined system can be solved for the elements by the method of least squares. We solve the over-determined system by computing its singular-value decomposition, which provides a quantitative measure of the "observability" of the matrix elements given a set of sensor coordinates, which define the coefficients $K_{ij}^{(k)}$. Such a sensitivity analysis can be used to optimize the spatial sampling of sensor data to provide the most robust estimate of the elements of \mathbf{S} . Ideally, we would like to position the sensor so that the incident magnetic field "views" the ordnance from many different directions.

References

1. Won, I.J., Keiswetter, D.A., Fields, G.R.A., and Sutton, L.C., 1996, GEM-2: A new multi-frequency electromagnetic sensor: *J. Env. Eng. Geophysics.*, v. 1, p. 129-137.

2. Won, I.J., Keiswetter, D.A., Hanson, D.R., Novikova, E., and Hall, T.M., 1997, GEM-3: A monostatic broadband electromagnetic induction sensor: *J. Env. Eng. Geophysics*, v. 2, p. 53-64.
3. Won, I.J., Keiswetter, D.A., and Novikova, E., 1998, Electromagnetic induction spectroscopy: *J. Env. Eng. Geophysics*, v. 3, p. 27-40.
4. Bell, T.H., Barrow, B., and Khadr, N., 1998, Shape-based classification and discrimination of subsurface objects using electromagnetic induction: *Proceedings of the International Geoscience and Remote Sensing Symposium (IGARSS)*, Seattle, WA.
5. Bell, T.H., Barrow, B.J., and Miller, J.T., 2000, Subsurface discrimination using electromagnetic induction sensors: *SPIE Proceedings*, v. 4129, p. 120-129.
6. Ozdemir, M., Miller, E.L., and Norton, S.J., 1998, Localization and characterization of buried objects from multi-frequency, array inductive data: *SPIE Proceedings*: Orlando, FL.
7. Das, Y., McFee, J.E., Toews, J., and Stuart, G.C., 1990, Analysis of an electromagnetic induction detector for real-time location of buried objects: *IEEE Trans. Geosci. Remote Sensing*, GRS-28, p. 278-288.
8. Baum, C.E. (Ed.), 1999, *Detection and identification of visually obscured targets*: Taylor and Francis, Philadelphia.
9. Burrows, M.L., 1964, *A Theory of Eddy-Current Flaw Detection*, PhD Thesis, University of Michigan.